Uniaxial Shear Strain as a Mechanism to Increase Spin Lifetime in Thin Film of a SOI-Based Silicon Spin FETs

Dmitri Osintsev, Viktor Sverdlov and Siegfried Selberherr

Abstract In this chapter we investigate spin relaxation in thin silicon films. We employ a **k**·**p** based approach to investigate surface roughness and phonon induced momentum and spin relaxation matrix elements. We show that the spin relaxation matrix elements strongly decrease with shear strain increased. In order to meet computational requirements with actual resources needed for relaxation time calculations, we demonstrate a way to find the subband wave function from the **k**·**p** model analytically. We consider the impact of the surface roughness and phonons on transport and spin characteristics in ultra-thin SOI MOSFET devices. We show that the regions in the momentum space responsible for strong spin relaxation can be efficiently removed by applying uniaxial shear strain. The spin lifetime in strained films can be improved by orders of magnitude.

1 Introduction

In order to achieve significant advantages in future microelectronic devices in comparison to present modern technology, operation principles will have to be enhanced or even modified. Spintronics is the rapidly developing technology promising to benefit from spin properties of electrons. Utilizing spin opens great opportunities to reduce device power consumption in future electronic circuits. A number of potential spintronic devices have already been proposed [1, 2]. Significant efforts are focused on developing models to study properties of future devices through simulation.

Silicon is the primary material for microelectronics. The long spin life time in silicon is a consequence of the weak intrinsic spin-orbit coupling in the conduction band and the spatial inversion symmetry of the lattice resulting in an absence of

D. Osintsev (✉) · V. Sverdlov · S. Selberherr
Institute for Microelectronics, TU Wien, Gußhausstraße 27–29/E360, A-1040 Wien, Austria
e-mail: osintsev@iue.tuwien.ac.at

A. Nazarov et al. (eds.), *Functional Nanomaterials and Devices for Electronics, Sensors and Energy Harvesting*, Engineering Materials,
DOI 10.1007/978-3-319-08804-4_7

Dresselhaus effective spin-orbit interaction [3, 4]. In addition, silicon is composed of nuclei with predominantly zero magnetic moment. A long spin transport distance of conduction electrons has already been demonstrated experimentally [5]. Spin propagation at such distances combined with a possibility of injecting spin at room temperature [6] or even elevated temperature [7] in silicon makes the fabrication of spin-based switching devices quite plausible in the upcoming future. However, the relatively large spin relaxation experimentally observed in electrically-gated lateral-channel silicon structures [3] might become an obstacle for realizing spin driven devices [4], and a deeper understanding of the fundamental spin relaxation mechanisms in silicon MOSFETs is urgently needed [8].

In this chapter we investigate the influence of the intrinsic spin-orbit interaction on the subband structure, subband wave functions, and spin relaxation matrix elements due to the surface roughness scattering in thin silicon films. We developed a semi-analytical approach allowing to analyze surface roughness and phonon induced spin and momentum relaxation in thin silicon films.

Following recent work [4], a **k**·**p** based method [9, 10] suitable to describe the electron subband structure in the presence of strain is generalized to include the spin degree of freedom. In contrast to [4], our effective 4×4 Hamiltonian considers only the relevant [001] oriented valleys with spin degree included, which produces the low-energy unprimed subband ladder. Within this model the unprimed subbands in the unstrained (001) film are degenerate, without spin-orbit effects included. An accurate inclusion of the spin-orbit interaction results in a large mixing between the spin-up and spin-down states, resulting in spin hot spots along the [100] and [010] axes characterized by strong spin relaxation. These hot spots should be contrasted with the spin hot spots appearing in the bulk system along the same directions at the edge of the Brillouin zone [4, 11]. The origin of the hot spots in thin films lies in the unprimed subband degeneracy which effectively projects the bulk spin hot spots from the edge of the Brillouin zone to the center of the 2D Brillouin zone.

Shear strain lifts the degeneracy between the unprimed subbands [10]. The energy splitting between the otherwise equivalent unprimed subbands removes the origin of the spin hot spots in a confined electron system in silicon, which substantially improves the spin lifetime in gated silicon systems.

2 Model

We numerically investigate the dependence of the matrix elements due to surface roughness induced spin relaxation in silicon films as a function of shear strain. For [001] oriented valleys in a (001) silicon film the Hamiltonian is written in the vicinity of the X point along the k_z-axis in the Brillouin zone. The basis is conveniently chosen as $[(X_1,\uparrow), (X_1,\downarrow), (X_{2'},\uparrow), (X_{2'},\downarrow)]$, where $\uparrow$ and $\downarrow$ indicate the spin projection at the quantization z-axis, X_1 and $X_{2'}$ are the basis function corresponding to the two valleys. The effective **k**·**p** Hamiltonian reads as

$$H = \begin{bmatrix} H_1 & H_3 \\ H_3^{\dagger} & H_2 \end{bmatrix}, \tag{1}$$

with H_1, H_2 and H_3 defined as

$$H_1 = \left[\frac{\hbar^2 k_z^2}{2m_l} - \frac{\hbar^2 k_0 k_z}{m_l} + \frac{\hbar^2 \left(k_x^2 + k_y^2\right)}{2m_t} + U(z) \right] I, \tag{2}$$

$$H_2 = \left[\frac{\hbar^2 k_z^2}{2m_l} + \frac{\hbar^2 k_0 k_z}{m_l} + \frac{\hbar^2 \left(k_x^2 + k_y^2\right)}{2m_t} + U(z) \right] I, \tag{3}$$

$$H_3 = \begin{bmatrix} D\varepsilon_{xy} - \frac{\hbar^2 k_x k_y}{M} & \left(k_y - k_x i\right)\Delta_{SO} \\ \left(-k_y - k_x i\right)\Delta_{SO} & D\varepsilon_{xy} - \frac{\hbar^2 k_x k_y}{M} \end{bmatrix}. \tag{4}$$

Here I is the identity 2×2 matrix, m_t and m_l are the transversal and the longitudinal silicon effective masses, $k_0 = 0.15 \times 2\pi/a$ is the position of the valley minimum relative to the X point in unstrained silicon, ε_{xy} denotes the shear strain component, $M^{-1} \approx m_t^{-1} - m_0^{-1}$, and $D = 14$ eV is the shear strain deformation potential. The spin-orbit term $\tau_y \otimes (k_x \sigma_x - k_y \sigma_y)$ with

$$\Delta_{so} = 2 \left| \sum \frac{\{X_1 | p_j | n\} \{n | [\nabla V \times p]_j | X_{2'}\}}{E_n - E_X} \right|, \tag{5}$$

couples states with the opposite spin projections from the opposite valleys. σ_x and σ_y are the spin Pauli matrices and τ_y is the y-Pauli matrix in the valley degree of freedom space. In the Hamiltonian (Eq. 1) $U(z)$ is the confinement potential, and the value $\Delta_{SO} = 1.27$ meVnm computed by the empirical pseudopotential method (Fig. 1) is close to the one reported by Li and Dery [4].

In the presence of strain and confinement the four-fold degeneracy of the n-th unprimed subband is partly lifted by forming an $n+$ and $n-$ subladder (the valley splitting), however, the degeneracy of the eigenstates with the opposite spin projections $n\pm \Uparrow\rangle$ and $n\pm \Downarrow\rangle$ within each subladder is preserved.

The degenerate states are chosen to satisfy

$$\langle \Uparrow n \pm | f | n \pm \Downarrow \rangle = 0, \tag{6}$$

with the operator f defined as

$$f = \cos\theta \sigma_z + \sin\theta \left(\cos\varphi \sigma_x + \sin\varphi \sigma_y\right), \tag{7}$$

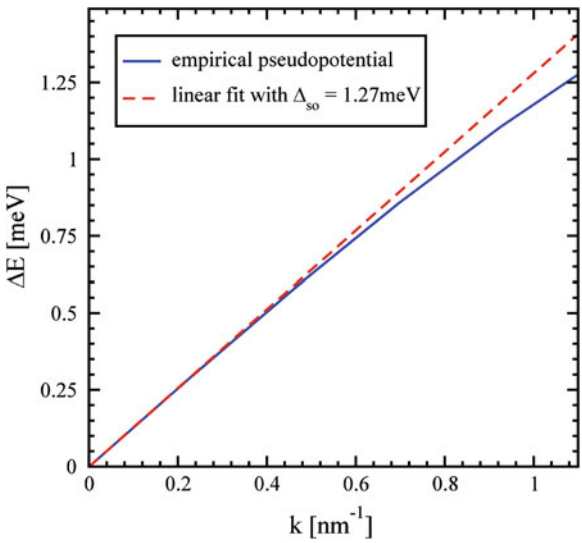

Fig. 1 Empirical pseudopotential calculations of the spin-orbit interaction strength by evaluating the gap opening at the X-point between X_1 and $X_{2'}$ for finite k_x

where θ is the polar and φ is the azimuth angle defining the orientation of the injected spin. In general, the expectation value of the operator f computed between the spin up and down states from different subladders is nonzero, when the effective magnetic field direction due to the spin-orbit interaction is different from the injected spin quantization axis

$$\bar{f} = \langle \Uparrow n \pm |f| n \mp \Downarrow \rangle \neq 0. \tag{8}$$

3 Valley Splitting

First we investigate the value of the energy splitting between the subbands with the same quantum number n but from different subsets $n+$ and $n-$ as a function of the conduction band offset at the interface, for different values of the quantum well thickness. In our calculations we assume the spin is injected along the z-direction and the components of the wave vector $\mathbf{k}$ are $k_x = 0.1$ nm^{-1} and $k_y = 0.1$ nm^{-1}. Figure 2 shows the subband splitting for three values of the film width, namely 1.36, 3.3, and 6.5 nm. Figure 2 demonstrates a complicated behavior which strongly depends on the thickness value, in contrast to the valley splitting theory in SiGe/Si/SiGe quantum wells [12], which predicts that in the case of a symmetric square well without an electric field the valley splitting is simply inversely proportional to the conduction band offset ΔE_c at the interfaces. Figure 2 shows that for the quantum well of 1.36 nm width the splitting first increases but later saturates. For the quantum well of 3.3 nm width a significant reduction of the valley splitting around the conduction band offset value 1.5 eV is observed. A further increase of the conduction band offset leads to an increase of the subband splitting

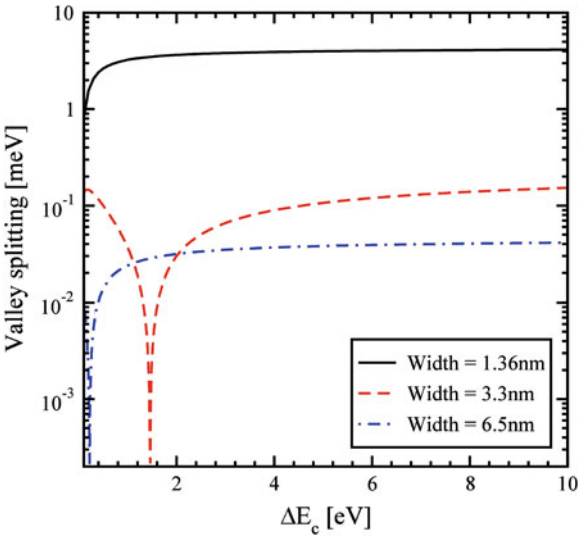

Fig. 2 Splitting between the lowest unprimed electron subbands as a function of the conduction band offset at the interface for different thicknesses for $\varepsilon_{xy} = 0$, $k_x = 0.1\ \text{nm}^{-1}$ and $k_y = 0.1\ \text{nm}^{-1}$

value. For the quantum well of 3.3 nm thickness the valley splitting saturates at about 0.17 meV.

For the quantum well of 6.5 nm width a significant reduction of the valley splitting is observed for a conduction band offset value 0.2 eV. The subband splitting saturates at a value 0.04 meV. Although for the values of the conduction band offset smaller than 4 eV the valley splitting depends on ΔE_c, for larger values of the conduction band offset it saturates.

The valley splitting dependence on strain as a function of the conduction band offset for the film of 3.3 nm thickness is shown in Fig. 3. Without shear strain the valley splitting is significantly reduced around the conduction band offset value of 1.5 eV. For the shear strain value of 0.25 and 0.5 % the sharp reduction of the conduction subbands splitting shifts to a smaller value of ΔE_c. However, the region of significant reduction is preserved even for the large shear strain value of 0.5 %. The value of the valley splitting at saturation for large shear strain is considerably enhanced as compared to the unstrained case.

The splitting of the lowest unprimed electron subbands as a function of the silicon film thickness for several values of the conduction band offset at the interfaces is shown in Fig. 4. The valley splitting oscillates with the film thickness increased. According to theory [9], we generalize the equation for the valley splitting in an infinite potential square well including the spin-orbit coupling as

$$\Delta E_n = \frac{2y_n^2 B}{k_0 t\sqrt{(1-y_n^2-\eta^2)(1-y_n^2)}}\left|\sin\left(\sqrt{\frac{1-y_n^2-\eta^2}{1-y_n^2}}k_0 t\right)\right|, \tag{9}$$

with y_n, η and B defined as

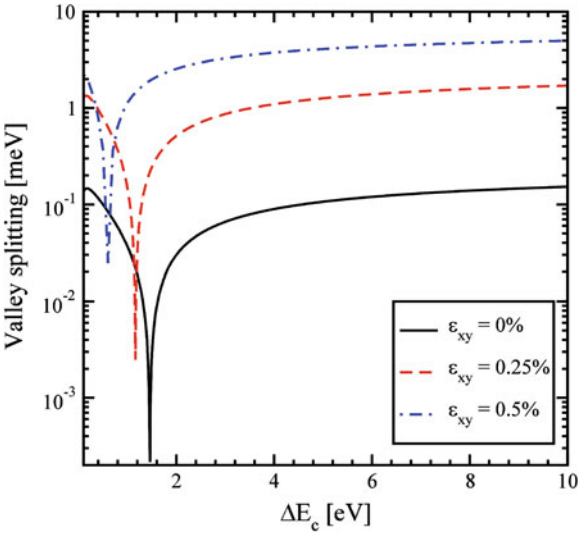

Fig. 3 Valley splitting as a function of the conduction band offset for the film thickness 3.3 nm for $k_x = 0.1$ nm^{-1} and $k_y = 0.1$ nm^{-1} for different shear strain values

$$y_n = \frac{\pi n}{k_0 t}, \tag{10}$$

$$\eta = \frac{m_l B}{\hbar^2 k_0^2}, \tag{11}$$

$$B = \sqrt{\Delta_{so}^2\left(k_x^2 + k_y^2\right) + \left(D\varepsilon_{xy} - \frac{\hbar^2 k_x k_y}{M}\right)^2}. \tag{12}$$

Here t is the film thickness. As it was shown earlier the conduction band value of 4 eV provides a subband splitting value close to the saturated one. Because Eq. 9 is written for an infinite potential square well, a slight discrepancy is observed between the theoretical curve and the numerically curve calculated for the conduction band offset value 4 eV in Fig. 4. A large value of the conduction band offset demonstrates a better agreement between the theory and numerically obtained results.

Following Eq. 9, the results shown in Fig. 2 can be understood as a consequence of vanishing of the $\left|\sin\left(\sqrt{\frac{1-y_n^2-\eta^2}{1-y_n^2}}k_0 t\right)\right|$ term. Although the conduction band offset is not included explicitly in the equation for the valley splitting, it can be taken into account trough an effective film width of a finite potential well as:

$$t_{\text{eff}} = t + \frac{2}{\alpha}, \tag{10}$$

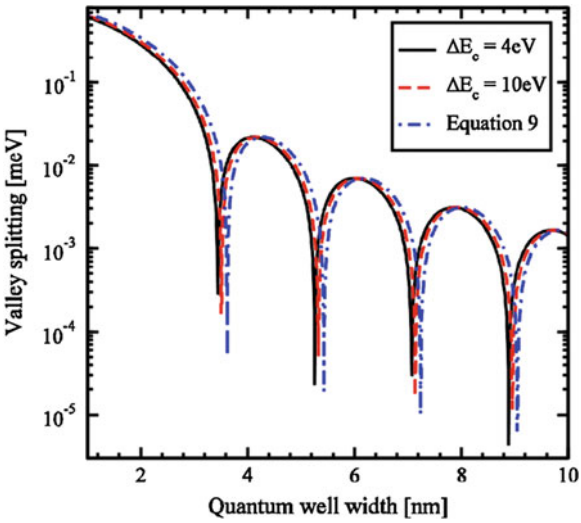

Fig. 4 Splitting of the lowest unprimed electron subbands as a function of the silicon film thickness for several values of the band offset at the interface, the shear strain value is 0.05 %, $k_x = 0.1\ \mathrm{nm}^{-1}$, $k_y = 0.2\ \mathrm{nm}^{-1}$

$$\alpha = \sqrt{\frac{2m(\Delta E_C - E)}{\hbar^2}}, \tag{11}$$

where E is the subband energy. Thus, increasing the potential barrier height leads to a decrease of the effective film thickness, which then results in the energy splitting dependence shown in Fig. 2.

The valley splitting reductions shown in Fig. 3 are also the result of the oscillating sine term in Eq. 9. The small increase of the shear strain leads to a decrease of the $\sqrt{\frac{1-y_n^2-\eta^2}{1-y_n^2}}$ term. This means that in order to obtain zeros of the sine term for larger shear strain values the effective quantum well thickness must be larger. A decrease in the conduction band offset leads precisely to such an increase of the effective thickness. Thus, the results shown in Fig. 3 are in very good agreement with theory.

Figure 5 shows the dependence of the energy splitting on shear strain for the in-plane wave vector $\boldsymbol{k}$ components are $k_x = 0.25\ \mathrm{nm}^{-1}$ and $k_y = 0.25\ \mathrm{nm}^{-1}$. The significant valley splitting reduction around the strain value 0.145 % appears to be independent of the quantum well width. According to Eq. 9, the valley splitting is also proportional to B, and the valley splitting reduction around the shear strain value 0.145 % is caused by vanishing of the $D\varepsilon_{xy} - \frac{\hbar^2 k_x k_y}{M}$ contribution. At this minimum the valley splitting is determined by the spin-orbit interaction term alone. The other valley splitting minima in Fig. 5 depend on the film thickness and are caused by vanishing values of the $\left|\sin\left(\sqrt{\frac{1-y_n^2-\eta^2}{1-y_n^2}}k_0 t\right)\right|$ term.

The valley splitting as a function of the quantum well width for different values of the effective electric field is shown in Fig. 6. Without electric field the valley splitting oscillates as shown in Fig. 4. With electric field the oscillations are not

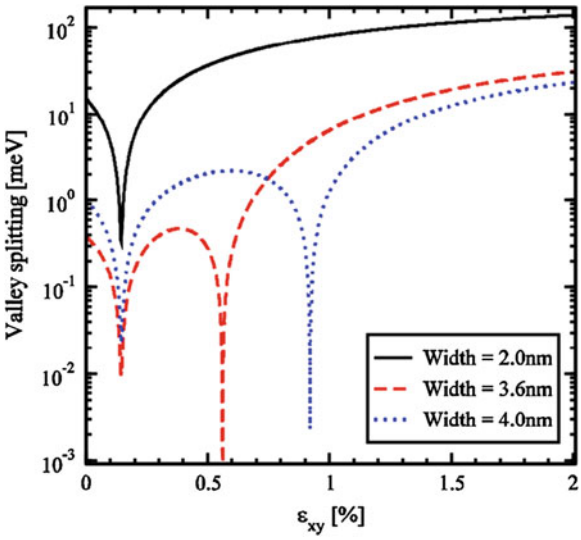

Fig. 5 Intervalley splitting as a function of shear strain for different values of the well width for $k_x = 0.25\ \text{nm}^{-1}$ and $k_y = 0.25\ \text{nm}^{-1}$

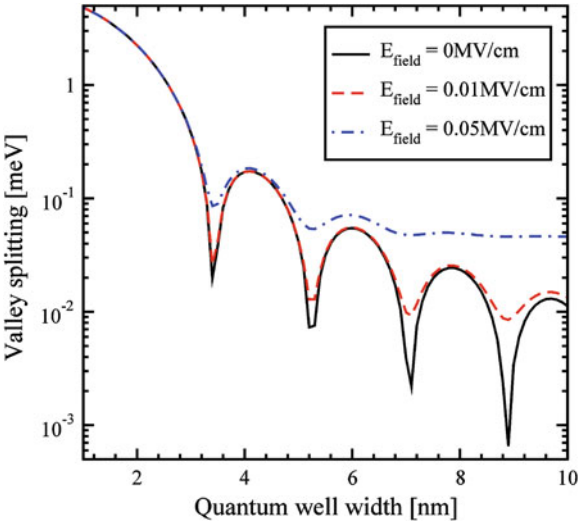

Fig. 6 Splitting of the lowest unprimed electron subbands as a function of the film thickness for different values of the effective electric field, the shear strain value is 0 %, the conduction band offset is 4 eV, $k_x = 0.1\ \text{nm}^{-1}$, $k_y = 0.1\ \text{nm}^{-1}$

observed in thicker films. This is due to the fact that in thick films the subband quantization is caused by the electric field. Indeed, for thin structures, when the quantization is still caused by the second barrier of the quantum well, the shape of the oscillations is similar to that in the absence of an electric field. According to [12], the condition for the independence of the valley splitting from the quantum well width is

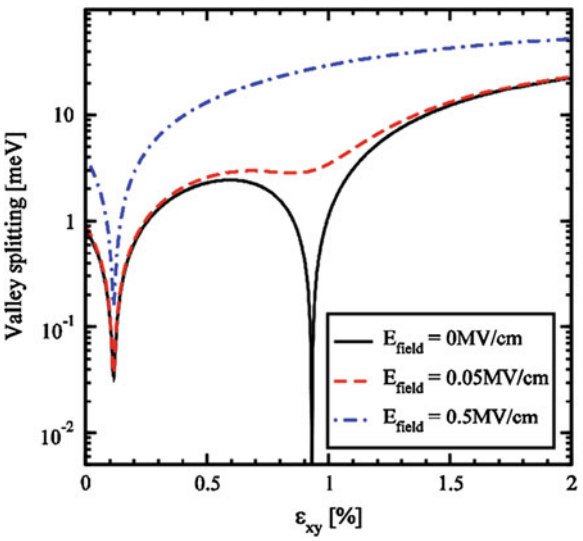

Fig. 7 Splitting of the lowest conduction subbands as a function of shear strain for different values of the electric field, the quantum well thickness is 4 nm, the conduction band offset is 4 eV, $k_x = 0.5\ \mathrm{nm}^{-1}$, $k_y = 0.1\ \mathrm{nm}^{-1}$

$$t^3 > \frac{2\pi^2\hbar^2}{m_l e E_{field}}. \tag{12}$$

For an electric field of 0.05 MV/cm the quantum well width must be larger than 6.9 nm in order to observe the valley splitting independent on the quantum well width. This value is in good agreement with the simulation results shown in Fig. 6.

Figure 7 shows the dependence of the valley splitting on strain. Without electric field the valley splitting reduces significantly around the strain values 0.116 and 0.931 % as shown in Fig. 7. With electric field applied the minimum around the strain value 0.931 % becomes smoother, however, for a strain value around 0.116 % the sharp reduction of the valley splitting is preserved. For large electric field the valley splitting reduction around the value 0.931 % vanishes completely.

For the strain value 0.116 % the sharp reduction of the valley splitting is still preserved at a minimum value only slightly affected by the electric field. As follows from Eq. 9, for $k_x = 0.5\ \mathrm{nm}^{-1}$, $k_y = 0.1\ \mathrm{nm}^{-1}$ the strain value 0.116 % causes the term $D\varepsilon_{xy} - \frac{\hbar^2 k_x k_y}{M}$ to vanish and minimizes the valley splitting, in good agreement with the first sharp valley splitting reduction in Fig. 7. Thus, the valley splitting at this strain value is solely determined by the spin-orbit interaction term. The second minimum in the valley splitting around the strain value 0.931 % in Fig. 7 is caused by vanishing of the $\left|\sin\left(\sqrt{\frac{1-y_n^2-\eta^2}{1-y_n^2}}k_0 t\right)\right|$ term. The effective electric field alters the confinement in the well and is therefore able to completely wash out the minimum in valley splitting due to the sine term. However, in agreement with Eq. 9, it can only slightly affect the first minimum due to the shear strain dependent contribution, in agreement with Fig. 7.

4 Scattering and Relaxation Matrix Elements Calculations

The surface roughness scattering matrix elements are proportional to the square of the product of the subband function derivatives at the interface [13]. The surface roughness at the two interfaces is assumed to be equal and statistically independent. It is described by a mean and a correlation length [13].

Figures 8 and 9 show the dependences on strain and electric field of the matrix elements for intrasubband and intersubband scattering due to surface roughness. The intrasubband scattering matrix elements have two decreasing features shown in Fig. 8. These features correlate with the valley splitting minima in Fig. 7. As in Fig. 7, for higher electric fields the second decreasing feature around the shear strain value of 0.9 % vanishes. For the electric field of 0.5 MV/cm the intrasubband matrix elements are sharply reduced only for the shear strain value of 0.116 %. At the same time, the intersubband matrix elements show a sharp increase around the shear strain value of 0.116 %. The electric field does not affect much the valley splitting provided by vanishing of the term $D\varepsilon_{xy} - \frac{\hbar^2 k_x k_y}{M}$, and the sharp increase in the inter-subband matrix elements is observed at higher fields as well.

Figures 10 and 11 show the dependence of the inter- and intrasubband spin relaxation matrix elements (normalized to the intravalley scattering at zero strain) on the angle between the incident and scattered wave vectors simultaneously with the valley splitting (calculated for the scattered wave vector value). As shown in Fig. 10, for small strain the sharp increases of the relaxation matrix elements are correlated with the minima in the valley splitting, which occur for the values of the angle determined by zeroes of the $D\varepsilon_{xy} - \frac{\hbar^2 k_x' k_y'}{M}$ term. This is the condition of the formation of the so called spin hot spots characterized by large spin mixing and

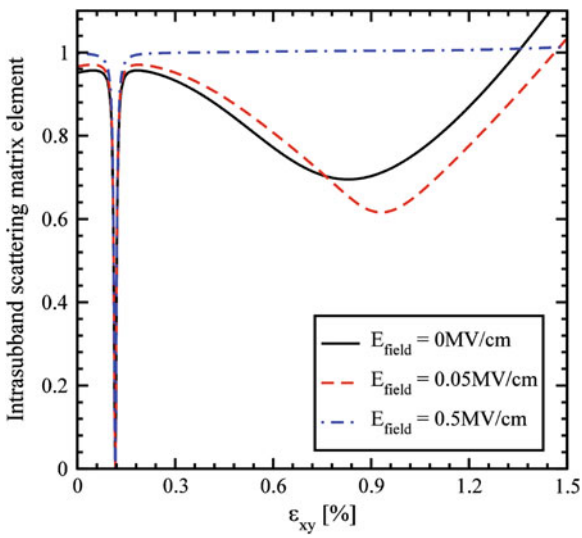

Fig. 8 Intravalley scattering matrix elements normalized by their values for zero strain as a function of shear strain for different electric field values

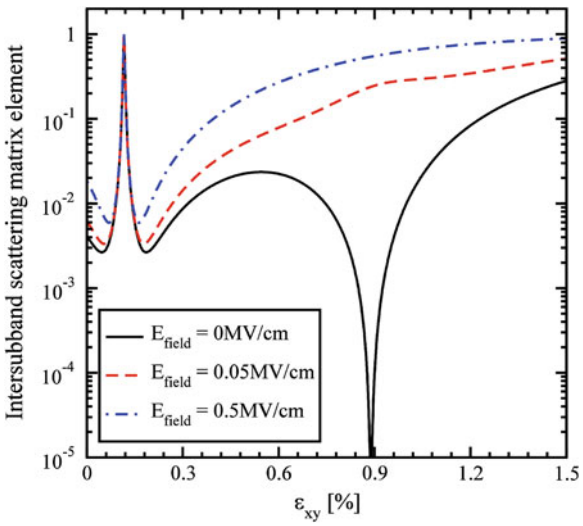

Fig. 9 Intervalley scattering matrix elements normalized to the value of the intravalley scattering at zero strain as a function of strain for different electric field values

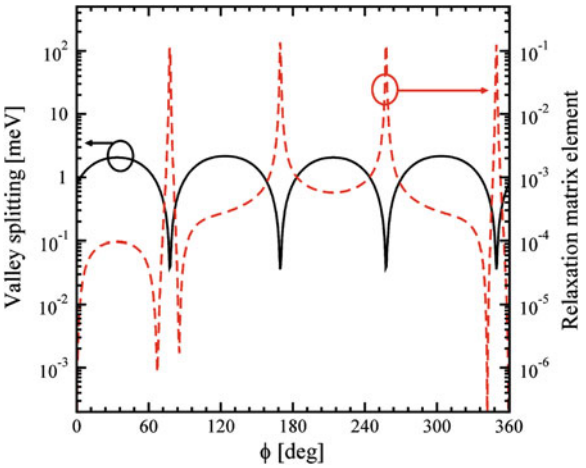

Fig. 10 Dependence of the normalized spin relaxation matrix elements and valley splitting on the angle between the incident and scattered waves for the quantum well thickness is 4 nm, the conduction band offset is 4 eV, $k_x = 0.5$ nm^{-1}, $k_y = 0.1$ nm^{-1}, $E_{field} = 0$ MV/cm, $\varepsilon_{xy} = 0.01$ %

relaxation. For higher shear strain values, however, the condition $D\varepsilon_{xy} - \frac{\hbar^2 k_x' k_y'}{M} = 0$ cannot be satisfied. In this case the valley splitting reduction shown in Fig. 11 is due to $\left|\sin\left(\sqrt{\frac{1-y_n^2-\eta^2}{1-y_n^2}}k_0 t\right)\right| = 0$, in contrast to Fig. 10. Correspondingly, these

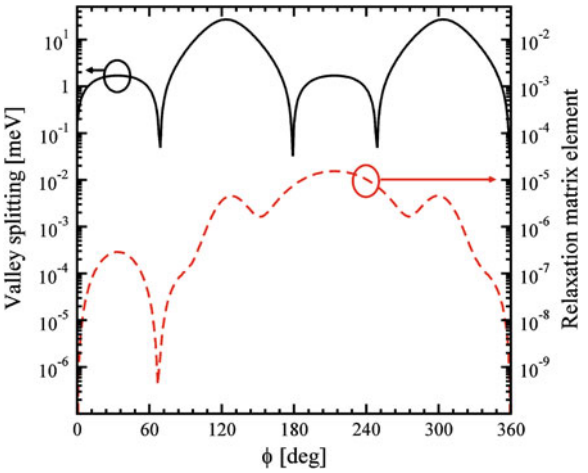

Fig. 11 Dependence of the normalized spin relaxation matrix elements and valley splitting on the angle between the incident and scattered waves for the quantum well thickness is 4 nm, the conduction band offset is 4 eV, $k_x = 0.5$ nm^{-1}, $k_y = 0.1$ nm^{-1}, $E_{field} = 0$ MV/cm, $\varepsilon_{xy} = 0.92$ %

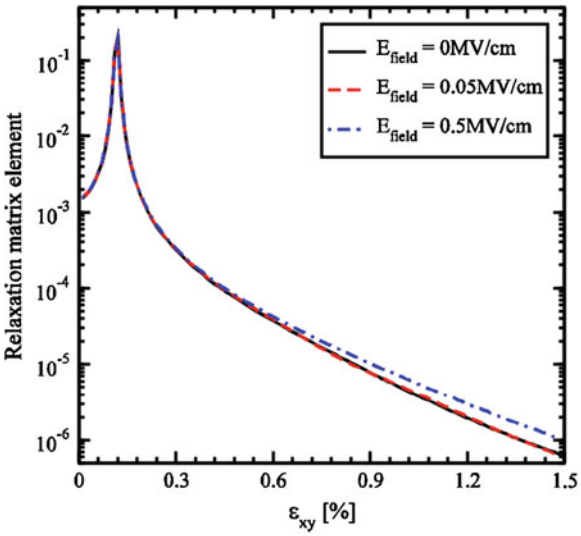

Fig. 12 Spin relaxation matrix elements normalized to intravalley scattering at zero strain dependence on shear strain for several values of the electric field, $k_x = 0.5$ nm^{-1}, $k_y = 0.1$ nm^{-1}

valley splitting minima do not result in sharp increases in the spin relaxation matrix elements on the angle between the incident and scattered waves.

The dependence of the intersubband spin relaxation matrix elements on shear strain for several values of the electric field is shown in Fig. 12. The spin

relaxation increases up to the strain value 0.116 %, the point determined by the spin hot spot condition. Applying strain larger than 0.116 % suppresses spin relaxation significantly, for all values of the electric field. In contrast to the scattering matrix elements (Figs. 8 and 9), the relaxation matrix elements demonstrate a sharp feature only for the shear strain value of 0.116 %. Large electric fields lead to an increase of the spin relaxation matrix elements due to the additional field-induced confinement.

5 Spin Relaxation

We are considering three mechanisms which contribute to the spin and momentum relaxation: surface roughness (SR), intra- and intervalley (for spin relaxation) scattering by acoustic phonons.

The spin and momentum relaxation times are calculated by thermal averaging [4, 8, 13] as

$$\frac{1}{\tau} = \frac{\int \frac{1}{\tau(\mathbf{K}_1)} f(\varepsilon)(1 - f(\varepsilon)) \mathrm{d}\mathbf{K}_1}{\int f(\varepsilon) \mathrm{d}\mathbf{K}_1}, \tag{13}$$

$$\int \mathrm{d}\mathbf{K}_1 = \int_0^{2\pi} \int_0^{\infty} \frac{|\mathbf{K}_1|}{\left|\frac{\partial \varepsilon(\mathbf{K}_1)}{\partial \mathbf{K}_1}\right|} \mathrm{d}\varphi \mathrm{d}\varepsilon. \tag{14}$$

The surface roughness momentum (spin) relaxation rate is calculated in the following way

$$\begin{aligned} \frac{1}{\tau_{SR}(\mathbf{K}_1)} = & \frac{2(4)\pi}{\hbar(2\pi)^2} \sum_{i,j} \int_0^{2\pi} \pi \Delta^2 L^2 \frac{1}{\epsilon_{ij}^2(\mathbf{K}_2 - \mathbf{K}_1)} \frac{\hbar^4}{4m_l^2} \frac{|\mathbf{K}_2|}{\left|\frac{\partial \varepsilon(\mathbf{K}_2)}{\partial \mathbf{K}_2}\right|} \\ & \times \left[\left(\frac{d\Psi_{i\mathbf{K}_1\sigma}}{dz} \right)^* \frac{d\Psi_{j\mathbf{K}_2-\sigma}}{dz} \right]_{z=\pm\frac{t}{2}}^2 \exp\left(\frac{-(\mathbf{K}_2 - \mathbf{K}_1)^2 L^2}{4} \right) \mathrm{d}\varphi, \end{aligned} \tag{15}$$

where ε is the electron energy, $K_{1,2}$ are the in-plane wave vectors before and after scattering, φ is the angle between K_1 and K_2, ε_{ij} is the dielectric permittivity, L is the autocorrelation length, Δ is the mean square value of the surface roughness fluctuations, $\Psi_{i\mathbf{K}_1}$ and $\Psi_{j\mathbf{K}_2}$ are the wave functions, and $f(\varepsilon)$ is the Fermi function, and $\sigma = +1$ is the spin projection to the [001] axis.

The momentum relaxation time is evaluated in the standard way [13, 14]. The spin relaxation rate due to the transversal acoustic phonons is calculated as

$$\frac{1}{\tau_{TA}(\mathbf{K}_1)} = \frac{4\pi k_B T}{\hbar \rho v_{TA}^2} \sum \int_0^{2\pi} \frac{d\varphi}{2\pi} \frac{|\mathbf{K}_2|}{\left|\frac{\partial \varepsilon(\mathbf{K}_2)}{\partial \mathbf{K}_2}\right|} \left[1 - \frac{\frac{\partial \varepsilon(\mathbf{K}_2)}{\partial \mathbf{K}_2} f(\varepsilon(\mathbf{K}_2))}{\frac{\partial \varepsilon(\mathbf{K}_1)}{\partial \mathbf{K}_1} f(\varepsilon(\mathbf{K}_1))}\right] \frac{1}{2}$$
$$\times \int_0^t \int_0^t \exp\left(-\sqrt{q_x^2 + q_y^2}|z - z'|\right) \left[\Psi^{\dagger}_{\mathbf{K}_2 - \sigma}(z) M \Psi_{\mathbf{K}_1 \sigma}(z)\right]^*$$
$$\times \left[\Psi^{\dagger}_{\mathbf{K}_2 - \sigma}(z') M \Psi_{\mathbf{K}_1 \sigma}(z')\right] \left[\sqrt{q_x^2 + q_y^2} - \frac{8 q_x^2 q_y^2 - \left(q_x^2 + q_y^2\right)^2}{q_x^2 + q_y^2} |z - z'|\right] dz dz', \tag{16}$$

where k_B is the Boltzmann constant, T is the temperature, $\rho = 2{,}329$ kg/m^3 is the silicon density, $\upsilon_{TA} = 5{,}300$ m/s is the transversal phonons velocity, $(q_x, q_y) = K_1 - K_2$ and M is the 4×4 matrix written in the basis for the spin relaxation rate.

$$M = \begin{bmatrix} 0 & 0 & \frac{D}{2} & 0 \\ 0 & 0 & 0 & \frac{D}{2} \\ \frac{D}{2} & 0 & 0 & 0 \\ 0 & \frac{D}{2} & 0 & 0 \end{bmatrix}. \tag{17}$$

Here $D = 14$ eV is the shear deformation potential.

The intravalley spin relaxation rate due to the longitudinal acoustic phonons is calculated as

$$\frac{1}{\tau_{LA}(\mathbf{K}_1)} = \frac{4\pi k_B T}{\hbar \rho v_{LA}^2} \sum \int_0^{2\pi} \frac{d\varphi}{2\pi} \frac{|\mathbf{K}_2|}{\left|\frac{\partial \varepsilon(\mathbf{K}_2)}{\partial \mathbf{K}_2}\right|} \left[1 - \frac{\frac{\partial \varepsilon(\mathbf{K}_2)}{\partial \mathbf{K}_2} f(\varepsilon(\mathbf{K}_2))}{\frac{\partial \varepsilon(\mathbf{K}_1)}{\partial \mathbf{K}_1} f(\varepsilon(\mathbf{K}_1))}\right] \frac{1}{2}$$
$$\times \int_0^t \int_0^t \exp\left(-\sqrt{q_x^2 + q_y^2}|z - z'|\right) \left[\Psi^{\dagger}_{\mathbf{K}_2 - \sigma}(z) M \Psi_{\mathbf{K}_1 \sigma}(z)\right]^*$$
$$\times \left[\Psi^{\dagger}_{\mathbf{K}_2 - \sigma}(z') M \Psi_{\mathbf{K}_1 \sigma}(z')\right] \frac{4 q_x^2 q_y^2}{\left(\sqrt{q_x^2 + q_y^2}\right)^3} \left[\sqrt{q_x^2 + q_y^2}|z - z'| + 1\right] dz dz', \tag{18}$$

Here $\upsilon_{LA} = 8{,}700$ m/s is the speed of the longitudinal phonons and the matrix M is defined with Eq. 17.

The intervalley spin relaxation rate contains the Elliot and Yafet contributions [8], which are calculated in the following way

$$\frac{1}{\tau_{LA}(\mathbf{K}_1)} = \frac{4\pi k_B T}{\hbar \rho v_{LA}^2} \sum \int_0^{2\pi} \frac{d\varphi}{2\pi} \frac{|\mathbf{K}_2|}{\left|\frac{\partial \varepsilon(\mathbf{K}_2)}{\partial \mathbf{K}_2}\right|} \left[1 - \frac{\frac{\partial \varepsilon(\mathbf{K}_2)}{\partial \mathbf{K}_2} f(\varepsilon(\mathbf{K}_2))}{\frac{\partial \varepsilon(\mathbf{K}_1)}{\partial \mathbf{K}_1} f(\varepsilon(\mathbf{K}_1))}\right] \times \frac{1}{2} \int_0^t \left[\Psi^{\dagger}_{\mathbf{K}_2-\sigma}(z) M' \Psi_{\mathbf{K}_1\sigma}(z)\right]^* \left[\Psi^{\dagger}_{\mathbf{K}_2-\sigma}(z) M' \Psi_{\mathbf{K}_1\sigma}(z)\right] dz. \tag{19}$$

Here the matrix M' is written as

$$M' = \begin{bmatrix} M_{ZZ} & M_{SO} \\ M_{SO}^{\dagger} & M_{ZZ} \end{bmatrix}. \tag{20}$$

$$M_{ZZ} = \begin{bmatrix} D_{ZZ} & 0 \\ 0 & D_{ZZ} \end{bmatrix}. \tag{21}$$

$$M_{SO} = \begin{bmatrix} 0 & D_{SO}(r_y - ir_x) \\ D_{SO}(-r_y - ir_x) & 0 \end{bmatrix}. \tag{22}$$

$(r_x,r_y) = K_1 + K_2$, $D_{zz} = 12$ eV, and $D_{SO} = 15$ meV/k$_0$ with $k_0 = 0.15 \times 2\pi/a$ defined as the position of the valley minimum relative to the X-point in unstrained silicon [8].

6 Wave Function Evaluation

Because of the spin hotspots determining the strong dependence of the spin relaxation scattering matrix elements on the relative angle between the incoming and scattered waves the assumption of the independence of the subband wave functions on the in-plane momentum frequently employed to estimate momentum relaxation cannot be used to evaluate the spin lifetime. Indeed, because spin-orbit effects are linear in in-plane momentum, the calculation of the surface roughness scattering matrix elements at the center of the 2D Brillouin zone usually performed for mobility calculations would result in the complete loss of all the effects due to spin-orbit interaction. Therefore, in order to accurately compute the spin lifetime numerically, one needs to know the subband wave functions as a function of the in-plane wave vector. Numerical evaluation of the wave functions with subsequent integration makes the task prohibitively expensive. To simplify the problem, we obtain the wave functions in a semi-analytical manner. For this purpose we rotate the Hamiltonian (Eq. 1) by means of the following unitary transformation. The four basis functions $X_{1\uparrow}$, $X_{1\downarrow}$, $X_{2\uparrow}$', $X_{2\downarrow}$', for the two [001] valleys with spin up, spin down are transformed by Eqs. 23–30 with $\tan(\Theta) = \frac{\Delta_{SO}\sqrt{k_x^2+k_y^2}}{D\varepsilon_{xy} - \frac{\hbar^2 k_x k_y}{M}}$. The transformation effectively decouples the spins with opposite direction in different valleys.

$$\Psi_1 = \frac{1}{2}\left[\left(X_{1\uparrow} + X'_{2\uparrow}\right) + \left(X_{1\downarrow} + X'_{2\downarrow}\right)\frac{k_x - ik_y}{\sqrt{k_x^2 + k_y^2}}\right], \tag{23}$$

$$\Psi_2 = \frac{1}{2}\left[\left(X_{1\uparrow} + X'_{2\uparrow}\right) - \left(X_{1\downarrow} + X'_{2\downarrow}\right)\frac{k_x - ik_y}{\sqrt{k_x^2 + k_y^2}}\right], \tag{24}$$

$$\Psi_3 = \frac{1}{2}\left[\left(X_{1\uparrow} - X'_{2\uparrow}\right) + \left(X_{1\downarrow} - X'_{2\downarrow}\right)\frac{k_x - ik_y}{\sqrt{k_x^2 + k_y^2}}\right], \tag{25}$$

$$\Psi_4 = \frac{1}{2}\left[\left(X_{1\uparrow} - X'_{2\uparrow}\right) - \left(X_{1\downarrow} - X'_{2\downarrow}\right)\frac{k_x - ik_y}{\sqrt{k_x^2 + k_y^2}}\right], \tag{26}$$

$$\mathrm{X}_1 = \Psi_1 \cos\left(\frac{\Theta}{2}\right) - i\Psi_3 \sin\left(\frac{\Theta}{2}\right), \tag{27}$$

$$\mathrm{X}_2 = \Psi_2 \cos\left(\frac{\Theta}{2}\right) + i\Psi_4 \sin\left(\frac{\Theta}{2}\right), \tag{28}$$

$$\mathrm{X}_3 = \Psi_3 \cos\left(\frac{\Theta}{2}\right) - i\Psi_1 \sin\left(\frac{\Theta}{2}\right), \tag{29}$$

$$\mathrm{X}_4 = \Psi_4 \cos\left(\frac{\Theta}{2}\right) + i\Psi_2 \sin\left(\frac{\Theta}{2}\right). \tag{30}$$

The Hamiltonian (Eq. 1) can now be cast into a form in which spins with opposite orientation in different valleys are independent

$$H = \begin{bmatrix} H_1 & H_3 \\ H_3 & H_2 \end{bmatrix}, \tag{31}$$

H_1, H_2 and H_3 are written as

$$H_1 = \left[\frac{\hbar^2 k_z^2}{2m_l} + \frac{\hbar^2\left(k_x^2 + k_y^2\right)}{2m_t} - \delta + U(z)\right] I, \tag{32}$$

$$H_2 = \left[\frac{\hbar^2 k_z^2}{2m_l} + \frac{\hbar^2\left(k_x^2 + k_y^2\right)}{2m_t} + \delta + U(z)\right] I, \tag{33}$$

$$H_3 = \begin{bmatrix} \frac{\hbar^2 k_0 k_z}{m_l} & 0 \\ 0 & \frac{\hbar^2 k_0 k_z}{m_l} \end{bmatrix}, \tag{34}$$

with $\delta = \sqrt{\left(D\varepsilon_{xy} - \frac{\hbar^2 k_x k_y}{M}\right)^2 + \Delta_{SO}^2\left(k_x^2 + k_y^2\right)}$.

Following [10] we find the wave functions analytically in the same manner as for the two-band $\mathbf{k} \cdot \mathbf{p}$ Hamiltonian written in the vicinity of the X point of the Brillouin zone for silicon films under uniaxial strain.

Figure 13 demonstrates an excellent agreement between the semi-analytical and the numerically obtained results for a silicon film of 4 nm thickness for the values $k_x = 0.25\ \mathrm{nm}^{-1}$ and $k_y = 0.25\ \mathrm{nm}^{-1}$. For the numerical calculations a barrier of 10 eV height has been assumed.

7 Results and Discussion

Figure 14 shows the dependence of the momentum relaxation time on temperature. The contributions from the surface roughness (SR) and acoustic phonons (PH) are shown. For the film thicknesses 2.1 and 1.36 nm the contribution from the surface roughness is dominant at low temperatures. However, for a temperature around 280 K the contributions from the surface roughness and from the acoustic phonons for the film of thickness 2.1 nm are equal. Any further increase of temperature leads to higher values of the momentum relaxation time caused by acoustic phonons. Figure 14 shows that the dominant relaxation mechanism strongly depends on film thickness. The phonons limited momentum relaxation is characterized by much weaker thickness dependence and does not change significantly while the thickness decreases from 2.1 to 1.36 nm. The surface roughness limited momentum relaxation decreases by more than an order of magnitude because of the expected t^6 dependence [13, 15]. Thus, for the thickness 1.36 nm the surface roughness induced spin relaxation is the dominant mechanism for the whole range of considered temperatures.

Figure 15 shows the dependence of the different mechanisms of the momentum relaxation together with the total momentum relaxation time on shear strain. The improvement of the momentum relaxation time due to the shear strain is around 82 % for the film thickness of 2.1 nm and around 120 % for the film thickness 1.36 nm. The acoustic phonons limited momentum relaxation improves around 45 % for 2.1 nm and around 92 % for 1.36 nm. The surface roughness limited momentum relaxation time increases around 110 % for 2.1 nm and around 120 % for 1.36 nm. Because the SR mechanism is the dominant for the film thickness

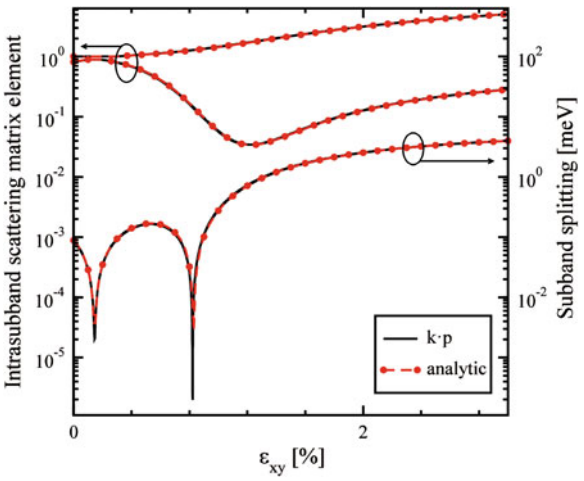

Fig. 13 Intrasubband scattering matrix elements normalized to their values at zero strain for the film thickness 1.36 nm for $k_x = 0.25$ nm^{-1} and $k_y = 0.25$ nm^{-1}, and subband splitting as a function of shear strain

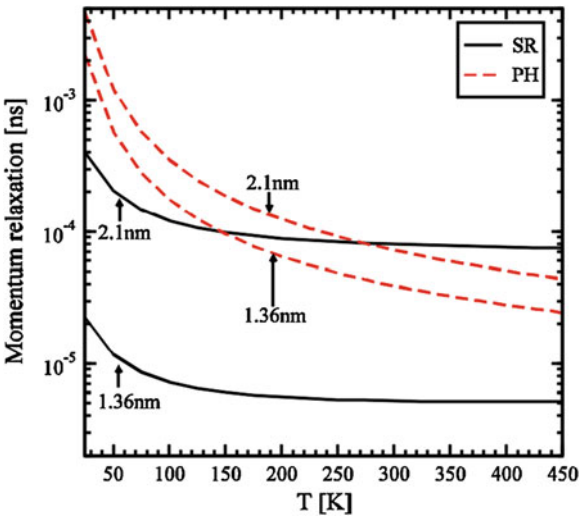

Fig. 14 Dependence of the momentum relaxation time induced by surface roughness (*SR*) and acoustic phonons (*PH*) on temperature for two different thicknesses, $\varepsilon_{xy} = 0$, and electron concentration 1.29×10^{12} cm^{-2}

1.36 nm, the increase of the total momentum relaxation time is higher for 1.36 nm than for 2.1 nm. We point out that the increase of the momentum relaxation time is due to the corresponding scattering matrix elements dependences' on strain. Combined with the strain induced transport effective mass decrease it should result in an even better mobility improvement supporting the use of uniaxial tensile strain as the mobility booster in fully depleted ultra-thin SOI FETs.

Figure 16 demonstrates the contribution of the inter- and intrasubband processes to the acoustic phonon and SR limited momentum relaxation. The domination of the intrasubband relaxation processes for both mechanisms of the momentum relaxation is shown, in agreement with the selection rule that the

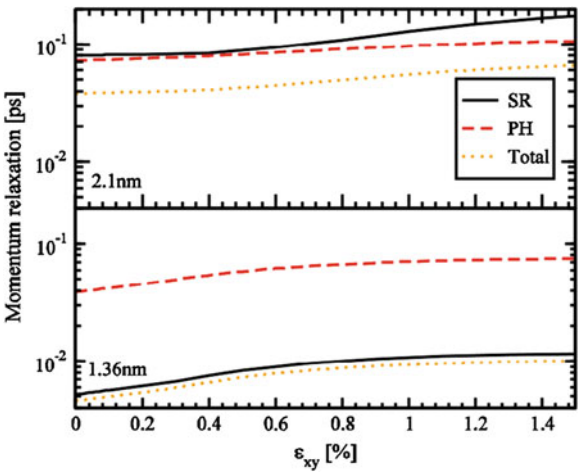

Fig. 15 Dependence of the momentum relaxation time induced by surface roughness (SR) and acoustic phonons (PH) on shear strain for 1.36 nm and 2.1 nm film thickness, for $T = 300$ K, and electron concentration 1.29×10^{12} cm^{-2}

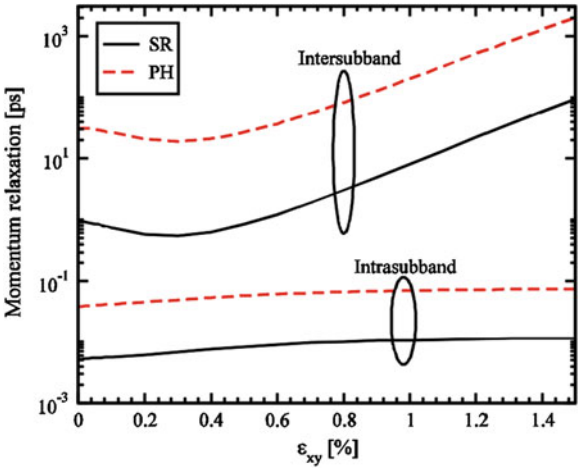

Fig. 16 Dependence of the intersubband and intrasubband components of the momentum relaxation time induced by surface roughness (*SR*) and acoustic phonons (*PH*) on shear strain for the film thickness 1.36 nm, $T = 300$ K, and electron concentration 1.29×10^{12} cm^{-2}

elastic processes result in strong intrasubband relaxation. The dominance of the SR mechanism for the film thickness 1.36 nm shown in Figs. 14 and 15 is the consequence of the high intrasubband relaxation rate.

The dependence of the spin lifetime on temperature for phonon scattering, and SR scattering for different carrier concentrations is shown in Fig. 17. The spin

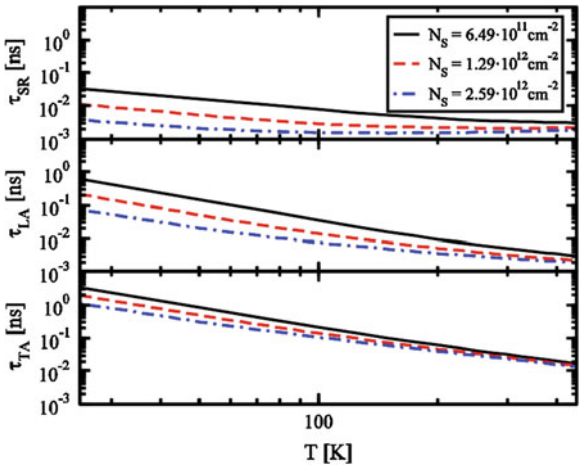

Fig. 17 Dependence of the surface roughness (*SR*), the longitudinal phonons' (*LA*), and the transversal phonons' (*TA*) contribution to the spin lifetime on temperature for different values of the electron concentration, for $\varepsilon_{xy} = 0$, and film thickness 2.1 nm

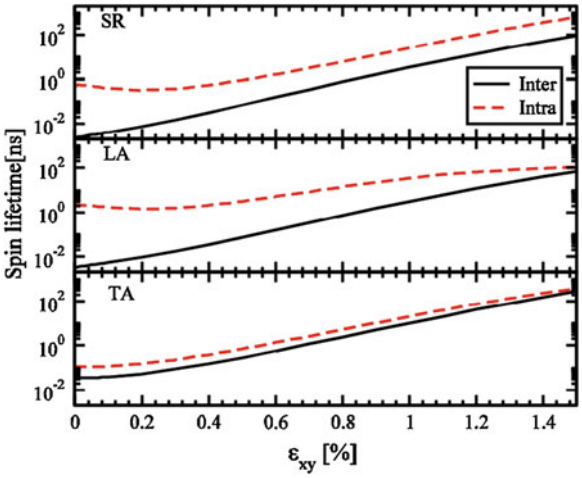

Fig. 18 Dependence of the intersubband and the intrasubband component of the spin lifetime for different spin relaxation mechanisms (surface roughness (*SR*), longitudinal phonons (*LA*), and transversal phonons (*TA*)) on shear strain for the film thickness 1.36 nm, $T = 300$ K, and electron concentration 1.29×10^{12} cm^{-2}

relaxation is more efficient for higher carrier concentrations for all three considered mechanisms. While the temperature increases, the difference between the spin lifetimes for different values of the electron concentration becomes less pronounced. Figure 17 shows that the SR mechanism dominates for all concentration

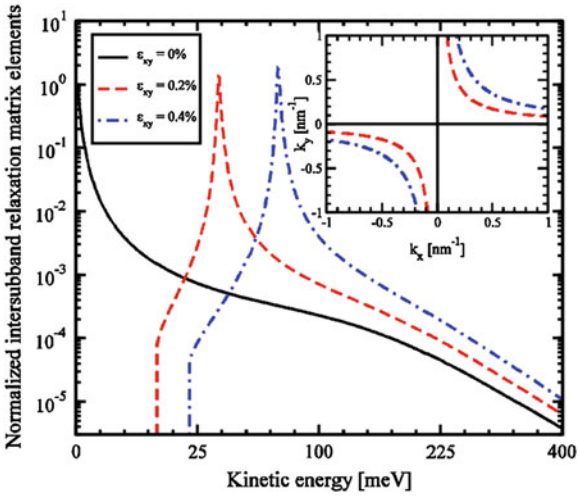

Fig. 19 Normalized intersubband relaxation matrix elements as a function of the conduction electrons kinetic energy in [110] direction. The *inset* shows the positions of the hot spots for different values of shear strain

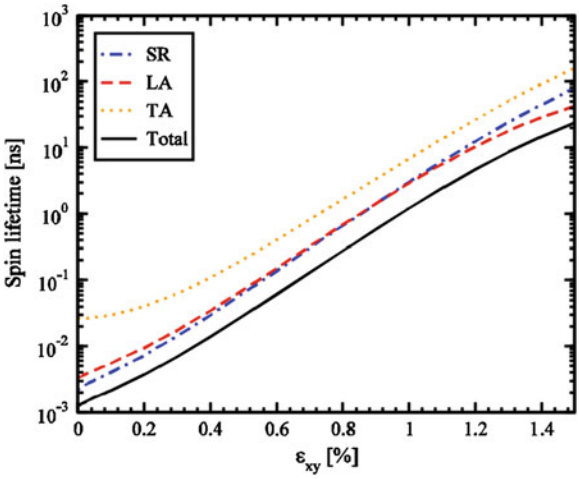

Fig. 20 Dependence of the spin lifetime on shear strain for the film thickness 2.1 nm, $T = 300$ K, and electron concentration 1.29×10^{12} cm^{-2}

values. Spin relaxation due to TA phonons is weakest among the three considered mechanisms.

Figure 18 demonstrates that the main contribution to spin relaxation comes from the intersubband processes due to the presence of the spin hot spots characterized by the sharp peaks of the intersubband spin relaxation matrix elements. Their position is shown in Fig. 19. For higher shear strain values the hot spots are pushed to higher energies away from the subband minima (inset in Fig. 19). This results in a strong increase of the spin lifetime with shear strain for SR and the phonon mechanisms as shown in Fig. 20.

8 Conclusion

We have included the spin-orbit interaction effects into the effective low-energy **k**·**p** Hamiltonian to investigate the valley splitting, scattering, and spin relaxation induced by the surface roughness and phonons in a thin film SOI MOSFET in a wide range of parameters. We have demonstrated that the valley splitting minima due to zero values of the sine term can be removed by the electric field, but the minimum due to the vanishing $D\varepsilon_{xy} - \frac{\hbar^2 k_x k_y}{M}$ term is preserved even for large electric fields. We have found that, due to the inter-subband splitting increase, the matrix elements for spin relaxation decrease rapidly with shear strain. To evaluate the wave function dependence on the in-plane momentum and spin relaxation time the **k**·**p** Hamiltonian is solved analytically. We have shown that by applying shear strain the momentum relaxation time can be improved by almost a factor of two for ultra-thin films. We have demonstrated a strong, several orders of magnitude, increase of spin lifetime in strained silicon films. Thus shear strain used to boost mobility can also be used to increase spin lifetime.

Acknowledgments This work is supported by the European Research Council through the grant #247056 MOSILSPIN. The computational results have been achieved using the Vienna Scientific Cluster (VSC).

References

1. Sugahara, S., Nitta, J.: Spin transistor electronics: an overview and outlook. Proc. IEEE **98**(12), 2124–2154 (2010)
2. Datta, S., Das, B.: Electronic analog of the electro-optic modulator. Appl. Phys. Lett. **56**, 665 (1990)
3. Li, J., Appelbaum, I.: Modeling spin transport in electrostatically-gated lateral-channel silicon devices: role of interfacial spin relaxation. Phys. Rev. B **84**, 165318 (2011)
4. Li, P., Dery, H.: Spin-orbit symmetries of conduction electrons in silicon. Phys. Rev. Lett. **107**, 107203 (2011)
5. Huang, B., Monsma, D.J., Appelbaum, I.: Coherent spin transport through a 350 Micron thick silicon wafer. Phys. Rev. Lett. **99**, 177209 (2007)
6. Dash, S.P., Sharma, S., Patel, R.S., de Jong, M.P., Jansen, R.: Electrical creation of spin polarization in silicon at room temperature. Nature **462**, 491–494 (2009)
7. Li, C.H., Van't Erve, O.M.J., Jonker, B.T.: Electrical injection and detection of spin accumulation in silicon at 500 K with magnetic metal/silicon dioxide contacts. Nat. Commun. **2**, 245 (2011)
8. Song, Y., Dery, H.: Analysis of phonon-induced spin relaxation processes in silicon. Phys. Rev. B **86**, 085201 (2012)
9. Bir, G.L., Pikus, G.E.: Symmetry and strain-induced effects in semiconductors. Wiley, New York (1974)
10. Sverdlov, V.: Strain-induced effects in advanced MOSFETs. Springer, Wien (2011)
11. Cheng, J.L., Wu, M.W., Fabian, J.: Theory of the spin relaxation of conduction electrons in silicon. Phys. Rev. Lett. **104**, 016601 (2010)

12. Friesen, M., Chutia, S., Tahan, C., Coppersmith, S.N.: Valley splitting theory of SiGe/Si/SiGe quantum wells. Phys. Rev. B **75**, 115318 (2007)
13. Fischetti, M.V., et al.: Six-band k·p calculation of hole mobility in silicon inversion layers: dependence on surface orientation, strain, and silicon thickness. J. Appl. Phys. **94**, 1079 (2003)
14. Fischetti, M.V., Laux, S.E.: Monte Carlo study of electron transport in silicon inversion layers. Phys. Rev. B **48**(4), 2244–2274 (1993)
15. Jin, S., Fischetti, M.V., Tang, T.: Modeling of electron mobility in gated silicon nanowires at room temperature: surface roughness scattering, dielectric scattering, and band nonparabolicity. J. Appl. Phys. **102**, 083715 (2007)